THE JOURNAL OF PHYSICAL CHEMISTRY C
A JOURNAL OF THE AMERICAN CHEMICAL SOCIETY

pubs.acs.org/JPCC

Article

Prediction of the TiS_2 Bilayer with Self-Intercalation: Robust Ferromagnetic Semiconductor with a High Curie Temperature

Fangyu Zhang, Linhui Lv, Zihao Xu, Diancong Qi, Weiyi Wang, Xingxing Li, Ya Su, Yanyan Jiang, and Zhaoyong Guan*

Cite This: https://doi.org/10.1021/acs.jpcc.4c06216

Read Online

ACCESS | Metrics & More | Article Recommendations | Supporting Information

ABSTRACT: The search for new two-dimensional magnetic materials has been a hot topic since the discovery of graphene in 2004 as these materials play a crucial role in fields such as spintronics. In this study, we systematically investigated the 2H-TiS_2 bilayer with self-intercalation (SI) of the Ti atom, revealing that SI can introduce magnetism to a nonmagnetic 2H-TiS_2. Taking $Ti_{19}S_{36}$-AB stacking as an example, we find that 2H−SI−TiS_2 exhibits a ferromagnetic order with a Curie temperature of 377 K. $Ti_{19}S_{36}$ shows perpendicular magnetic anisotropy, with a magnetic anisotropy energy (MAE) of 7.43 × 10^{-2} meV. Additionally, the MAE increases as the self-intercalated Ti's (Ti_{SI}) concentration (x) decreases, attributed to the enhanced hybridization interaction between the $d_{x^2-y^2}$ and d_{xy} orbitals of Ti atoms. $Ti_{19}S_{36}$-AB stacking is identified as a bipolar magnetic semiconductor (BMS) with an indirect band gap of 0.53 eV. As x increases, Ti_mS_n transitions from BMS to half-semiconductor (HSC) and metal and then back to HSC, demonstrating a rich phase. Ti_mS_n shows good dynamic and thermodynamic stabilities at 300 and 500 K, respectively. Furthermore, the formation energy (ε_f) of Ti_mS_n increases monotonically with rising x. Moreover, Ti_mS_n can be easily synthesized under higher μ_{Ti}. The migration barrier of Ti_{SI} between adjacent coordination sites is 0.740 eV, further confirming the stability of the self-intercalated structure. These findings imply the potential of 2H-TiS_2 and nonmagnetic transition metal dichalcogenides in spintronics.

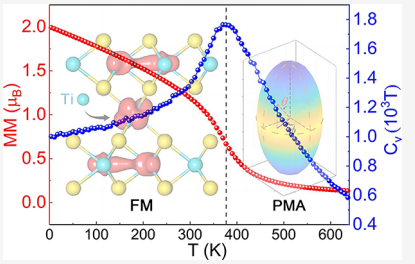

INTRODUCTION

The pursuit of undetected two-dimensional (2D) magnetic materials has garnered substantial interest since the landmark synthesis of graphene in 2004.[1,2] Recent breakthroughs have led to the discovery of intrinsic ferromagnetic (FM) order in materials, such as CrI_3,[3] Fe_3GeTe_2,[4] and $Cr_2Ge_2Te_6$,[5] marking significant strides in the study of 2D magnets. Experimental reports have predominantly focused on transition metal halides,[6,7] transition metal sulfides,[8,9] transition metal carbonitrides,[10] and transition metal phosphorus sulfides,[11] among others. These 2D magnetic materials exhibit diverse physicochemical properties that hold promise for applications in spintronics,[12,13] optoelectronics,[14,15] energy storage,[16,17] and information transfer.[18] In addition to that, 2D materials have recently been intensively explored as photocatalysts for water splitting[19] and as thermoelectric materials for producing green electricity.[20] Their ultrathin nature allows for modulating properties via external stimuli such as intercalation,[21−23] strain,[24−26] stacking order,[27,28] external electrical field,[2,29,30] and magnetic field,[5,31] thereby extending their application in 2D devices. Despite significant progress in obtaining intrinsic 2D magnetic materials through various methods, elucidating magnetic coupling mechanisms[32,33] and exploiting them to design materials with high transition temperatures remains a formidable challenge.[34]

Intercalation[35−37] emerges as a powerful strategy to modulate the properties of 2D materials. Intercalation offers a promising avenue for tailored modifications in electrical,[38] magnetic,[36,39] optical,[40] and catalytic[41] properties as van der Waals (vdW) interaction between layers. For instance, the Li atom's adsorption on CrI_3 surfaces transforms CrI_3 from an FM semiconductor to an FM half-metal.[42] A notable intercalation approach is self-intercalation (SI),[43−45] where native atoms within the material serve as intercalated agents. In 2020, Prof. Loh first achieved ultrathin covalently bonded materials through SI of bilayer (BL) transition metal disulfides (TMDs),[46] demonstrating adjustable intercalation concentrations ranging from 25 to 66.7%.

At present, much work has proven that SI can regulate the properties of BL structures in various aspects. The regulation of magnetism is an important direction.[47,48] When Cr atoms are self-intercalated into 2D Cr_xTe_y, the robust FM and strong perpendicular magnetic anisotropy (PMA) persist up to 210 K in the magnetic heterojunction because the SI plays a critical

Received: September 14, 2024
Revised: December 21, 2024
Accepted: December 26, 2024

role in the magnetic decoupling effect.[44] Our previous research also found that self-intercalated Mo atoms can introduce a long-range FM order to nonmagnetic 2H-MoS_2.[45] Besides, SI has a significant effect on the electronic structure. Wang et al. have directly visualized a stacking-selective SI phenomenon in epitaxial $Nb_{1+x}Se_2$ films.[49] It has been confirmed that SI can lower the density of states (DOS) at the Fermi level of $NbSe_2$, which in turn decreases the superconducting transition temperature. Employing molecular beam epitaxy (MBE), Zhang's team achieved the direct synthesis of an ultrathin Kagome-structured SI Co_9Te_{16}, which has a flat band near the Fermi level.[50] Moreover, SI can enhance the metallicity and chemical reactivity of materials, with certain intercalated 2D materials showing significant promise as hydrogen evolution reaction (HER) electrocatalysts.[51] These works show that SI can effectively regulate the diverse properties of TMDs.

Among TMDs, titanium disulfide (TiS_2) has been widely used in hydrogen storage[52] and high-density batteries[53] owing to its light weight, stability, and cost-effectiveness. TiS_2 has been extensively intercalated with various atoms including Na,[54] Ca,[55] Hg,[56] Cu,[57] Co,[58] and other transition metals (TMs).[59] Notably, self-intercalated compounds of TiS_2 have been synthesized for decades. The excess Ti atoms are incorporated into the vdW gap of TiS_2 due to the volatilization of sulfur atoms, leading to the formation of Ti_mS_n at high temperatures.[60] This controlled insertion of Ti atoms results in different electronic structures of Ti_mS_n.[61] Wang Han confirmed stoichiometric TiS_2 is a semiconductor with an indirect band gap of 0.5 eV.[62] Zhang Min achieved high-density Ti_mS_n (11.1%−16.1%) via a solid-state reaction combined with plasma-activated sintering.[60] However, systematic theoretical calculation of the properties of the 2H-TiS_2−SI structure is rare.

In this work, we systematically studied the geometries and magnetic and electronic properties of 2H−SI−TiS_2. The result shows that self-intercalated Ti (Ti_{SI}) can introduce magnetism into nonmagnetic TiS_2−BL. Ti_mS_n with x below 11.1% shows an FM order. The magnetic exchange mechanism of $Ti_{19}S_{36}$-AB stacking (11.1%) is investigated based on the Heisenberg model, and its Curie temperature (T_C) is estimated to be 377 K. Besides, $Ti_{19}S_{36}$ shows PMA, with a magnetic anisotropic energy (MAE) of 7.43×10^{-2}meV. The MAE monotonously increases as x decreases due to the enhanced hybridization interaction of the $d_{x^2-y^2}$ and d_{xy} orbitals of Ti atoms. In addition, $Ti_{19}S_{36}$ is a bipolar magnetic semiconductor (BMS) with an indirect band gap of 0.53 eV. As x increases, Ti_mS_n undergoes a transition from BMS to half-semiconductor (HSC) and metal and then back to HSC. Ti_mS_n exhibits good dynamic and thermodynamic stability at 300 and 500 K, respectively. Furthermore, the formation energy (ε_f) of Ti_mS_n increases monotonically with the x increasing. Ti_mS_n is easier to be synthesized under high μ_{Ti}. The migration barrier of Ti_{SI} between adjacent coordination sites is 0.740 eV, further verifying its structural stability. These findings provide a new path for introducing long-range FM ordering into nonmagnetic materials, demonstrating the potential of nonmagnetic materials in the field of spintronic devices.

Computing Method. In this work, the properties of Ti_mS_n are calculated using density functional theory and the Vienna ab initio simulation package (VASP).[63,64] The generalized gradient approximation[65] with the Perdew−Burke−Ernzerhof (PBE) functional is employed to describe the exchange-correlation potential. To account for the strong correlation effects of Ti's 3d electrons, both hybrid-functional HSE06[66] and LDA + U[67] methods are utilized. The Coulomb interaction parameter (U) and the exchange interaction parameter (J) are set to 4.00 eV[68] and 0.50 eV, respectively. Therefore, the effective U_{eff} is 3.50 eV. The LDA+U is used to calculate the phonon spectrum, geometry optimization, energies of various magnetic orders, band structure, DOS, and ab initio molecular dynamics (AIMD). The HSE06 functional is also used to verify the energies of different magnetic orders, band structures, and DOS. Spin−orbital coupling (SOC) is also considered in the calculation of MCA and band structure.

The convergence criteria for energy and Hellmann−Feynman forces during geometry optimization are set to 10^{-5} eV and 10^{-2} eV/Å, respectively. To avoid the virtual interaction, the vacuum distance on the c-axis is set to 16 Å. The kinetic energy cutoff is 360 eV. The Γ-centered Monkhorst−Pack[69] grids are 9 × 9 × 1, 6 × 6 × 1, 3 × 3 × 1, and 1 × 1 × 1 for the geometry optimization of Ti-intercalated TiS_2 BL with x of 100, 25, 11.1, and 6.25%, respectively. The x is defined as the ratio of the actual number to the number of all coordination sites.[46] The phonon spectra and DOS are calculated using the finite displacement method, implemented in the Phonopy package.[70] Band structure, DOS, and differential charge density are dealt with VASPKIT.[71] T_C is calculated using the PASP,[72] developed by Prof. Xiang. The constant-NVT ensemble with the Nosé−Hoover thermostat[73] is employed at temperatures of 300 and 500 K to verify the stability of the structures, in the AIMD simulation. To avoid unreasonable boundary conditions, we use a 2 × 2 × 1 supercell to simulate 10 ps with a time step of 1 fs. In addition to AIMD simulations, all other calculations are performed at 0 K. The climbing image nudged elastic band (CI-NEB)[74] method was used in the calculation of transfer barriers.

RESULTS AND DISCUSSION

Geometry. TiS_2 has a 2H phase structure with a space group of $P\bar{3}m1$. The layered TiS_2 consists of an octahedron of TiS_6, with each S being shared by three octahedrons, while the layers are connected by vdW interaction. The TiS_2 monolayer (ML) could be stripped by a combination of a lithium process and ultrasonic removal.[75] This study focuses on the SI structure of TiS_2 with AB stacking. The optimized structure of $Ti_{19}S_{36}$ with AB stacking presents an x of 11.11%, as shown in Figure 1. Initially, a Ti_{SI} atom is inserted into a 3 × 3 × 1 supercell of TiS_2 BL. The Ti_{SI} atom is in the centroid of the six nearest S atoms of BL. Each Ti atom is surrounded by an octahedron composed of six S atoms so that it still belongs to the D_{3d} point group, shown in Figure 1. The lattice parameters a and b expand slightly to 10.223 Å from the initial value of 10.212 Å due to the insertion of the Ti_{SI} atom, primarily in the plane direction. The distance between the two planes containing Ti atoms of the BL is 6.535 Å. The Ti−S bond lengths in the intercalated structure (denoted as d_1) and within the BL (denoted as d_2) are 2.605 and 2.515 Å, shown in Figure 1b. Moreover, six S atoms directly connected by the Ti_{SI} atom are 6 pm closer to Ti_{SI} in the c direction and six Ti atoms close to the Ti_{SI} atom are 0.6 pm closer to the Ti_{SI} atom in the c direction, shown in (see Supporting Information, Figure S1).

Magnetic Properties. In addition to the structural aspects, the magnetic properties of $Ti_{19}S_{36}$ were also investigated to explore the magnetic coupling mechanism. The magnetic moment (MM) predominantly localizes in the Ti_{SI} and the six

https://doi.org/10.1021/acs.jpcc.4c06216
J. Phys. Chem. C XXXX, XXX, XXX−XXX

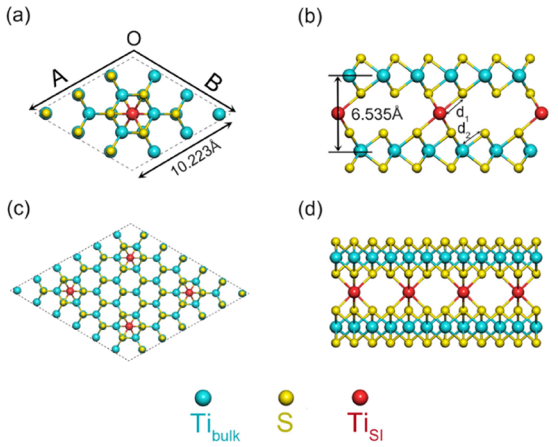

Figure 1. Illustration of the optimized geometries of $Ti_{19}S_{36}$-AB stacking (11.1%). (a) Top and (b) side views of the $Ti_{19}S_{36}$-AB structure. (c) Top and (d) side views of the $Ti_{19}S_{36}$-AB stacking with a 2 × 2 × 1 supercell.

nearest Ti atoms of the MLs. Different magnetic configurations are investigated: each Ti_{SI} contributes about 1.6 μ_B, while each of the surrounding six Ti atoms contributes 0.4 μ_B. We found that the spin orientations of the three atoms above or below the Ti_{SI} atom are constrained to be identical. Therefore, they are treated as a single entity, denoted as Ti_0, with a total MM of 1.2 μ_B, shown in Figure 2a. Six different magnetic orders were calculated. They are FM, Ferrim-I, Ferrim-II, Ferrim-III, AFM-I, and AFM-II orders, shown in Figure 2a–f, respectively. Ferrim-I order presents that Ti_{SI} atoms show FM coupling, and Ti_0 atoms in different layers show FM coupling. However, Ti_0 atoms in one layer have stripy-antiferromagnetic (AFM)[34] coupling, shown in Figure 2b. Ferrim-II order denotes FM coupling between all Ti_0, but stripy-AFM coupling is observed between Ti_{SI}, shown in Figure 2c. Ferrim-III order represents FM coupling between Ti_{SI} and FM coupling between Ti_0 in one layer. Conversely, Ti_0 in different layers shows AFM coupling, presented in Figure 2d. AFM-I order stands for FM coupling between Ti_0 in one layer. However, it has AFM coupling between Ti_0 in different layers, and stripy-AFM coupling between Ti_{SI}, depicted in Figure 2e. AFM-II order shows FM coupling between Ti_0 in different layers. However, it represents stripy-AFM between Ti_{SI} and stripy-AFM between Ti_0 in one layer, as shown in Figure 2f. The energy difference between six magnetic orders and the FM order reveals that the FM order has the lowest energy, shown in Figure 2. The energies from low to high are FM (corresponding to E_1), AFM-I (E_5), Ferrim-I (E_2), Ferrim-II (E_3), Ferrim-III (E_4), and AFM-II (E_6) orders, shown in Figure 2 (the explanation of FM order is provided in the following sections). Additionally, energies calculated by the hybrid functional corroborate those obtained from PBE+U calculations.

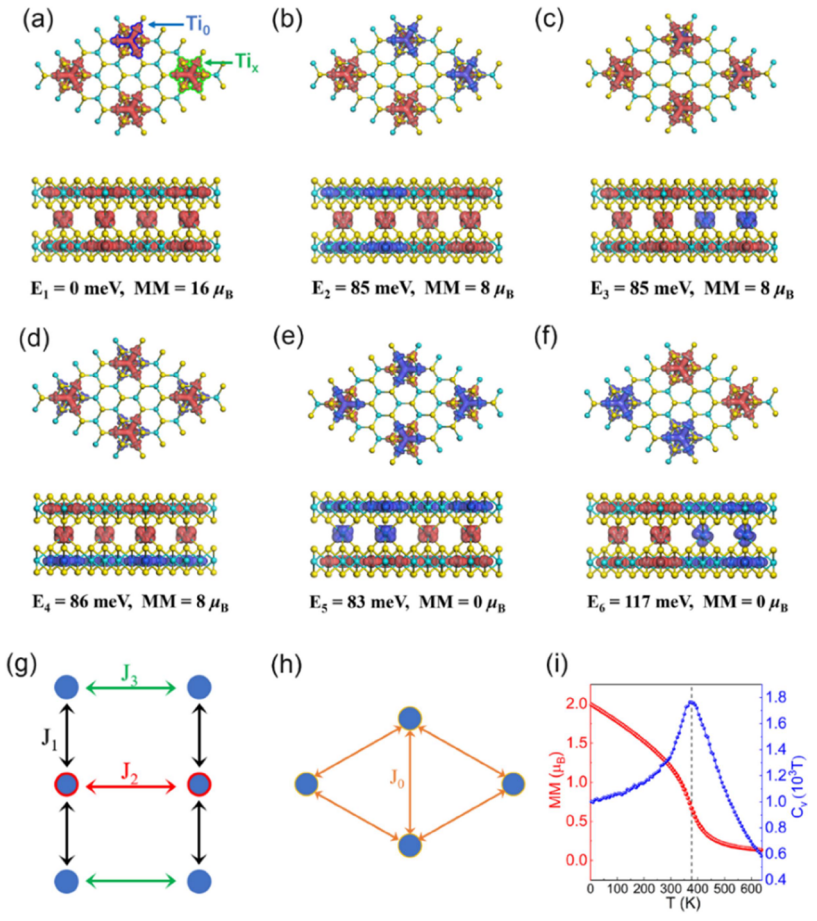

Figure 2. Spin charge densities of $Ti_{19}S_{36}$-AB stacking with (a) FM, (b) Ferrim-I, (c) Ferrim-II, (d) Ferrim-III, (e) AFM-I, and (f) AFM-II orders. The isovalue is set at 0.04 e/Å^3. (g) and (h) Schematic diagram of the defined magnetic exchange factor. (i) MM and heat capacity as a function of temperature in T_C simulation.

https://doi.org/10.1021/acs.jpcc.4c06216
J. Phys. Chem. C XXXX, XXX, XXX−XXX

To evaluate the T_C of $Ti_{19}S_{36}$, we examined the magnetic exchange constants, shown in Figure 2g. J_1 presents the first nearest-neighbor spin−spin exchange constant between Ti_0 and Ti_{SI}. J_2 represents the second nearest-neighbor spin−spin exchange constant between neighboring Ti_{SI}. J_3 shows the second nearest-neighbor spin−spin exchange constant between Ti_0 and other neighbor Ti_0 atoms, shown in Figure 2g. Positive J values indicate a dominant FM interaction, while negative values indicate a dominant AFM interaction. Based on the magnetic configurations shown in Figure 2a−d, we derived the following equations:

$$E_a = E_0 - 8J_1 - 12J_2 - 24J_3 \quad (1)$$

$$E_b = E_0 - 12J_2 + 8J_3 \quad (2)$$

$$E_c = E_0 + 4J_2 - 24J_3 \quad (3)$$

$$E_d = E_0 - 12J_2 - 24J_3 \quad (4)$$

The J_1, J_2, and J_3 are 10.375, 0.188, and 0.063 meV. J_1 is larger than J_2 and J_3, which shows that the FM coupling between Ti_{SI} and around six Ti atoms is the dominant factor. To estimate T_C, we consider seven Ti atoms as a whole with a 4.0 μ_B MM, denoted as Ti_x, and define the exchange interaction of the nearest neighbor as J_0, shown in Figure 2h. Based on magnetic orders, shown in Figure 2a,f, we derived the following equations:

$$E_a = E_0 - 12J_0 \quad (5)$$

$$E_f = E_0 + 4J_0 \quad (6)$$

J_0 is 7.313 meV. Then, we calculate T_C based on the Heisenberg model. The spin Hamiltonian can be described as

$$H = -\sum_{i<j} J_{ij} S_i \times S_j - \sum_i K_u (S_i^z)^2 \quad (7)$$

where J and S are the exchange constant and the spin operator, respectively. K_u and S_i^z represent the anisotropy constant and the spin orientation along the out-of-plane direction, respectively. In the later section, the MAE of $Ti_{19}S_{36}$ is calculated to be 0.0743 meV, which means K_u is 0.0743 meV (1% of the J_0). It implies that the influence of MAE on T_C is negligible. Therefore, the above formula can be simplified as

$$H = -\sum_{i<j} J_{ij} S_i \times S_j \quad (8)$$

In the calculation of T_C, the heat capacity first increases and reaches the largest value of 1.76×10^3T at a temperature of 377 K and then quickly goes down, as shown in Figure 2i. In addition, the slope of the MM curve also reaches the minimum at 377 K. Therefore, it can be concluded that the T_C is 377 K. It is clear that there is an inextricable relationship between the high T_C and the magnetic exchange constants dominated by FM coupling.

Differential Charge Density. TiS_2 ML and BL nonmagnetic semiconductor: Why could the Ti_{SI} atom introduce long-order FM? Ti belongs to the IV_B group of TM elements, with a valence electron configuration of $3d^2 4s^2$. The Ti atom in the TiS_2 bulk tends to lose four valence electrons, resulting in a filled closed-shell configuration. Consequently, there are almost no unpaired electrons, which makes it nonmagnetic. However, SI could act as localized charge doping.[45,76] This unsaturated Ti_{SI} atom introduces magnetism and spin states near the Fermi level.

We calculated the differential charge density of $Ti_{19}S_{36}$ to further elucidate the charge transfer introduced by the Ti_{SI} atom and explain the mechanism of FM coupling. The differential charge density after the introduction of the Ti_{SI} atom in $Ti_{19}S_{36}$ is shown in Figure 3a,b. Ti atoms can be classified into three categories: Ti_{SI}, Ti atoms adjacent to the intercalated layer (Ti_1, Ti_2, Ti_3), and remaining Ti atoms in the BL, as shown in Figure 3b. Charge transfer primarily occurs between Ti_{SI} and adjacent Ti atoms (Ti_1, Ti_2, and Ti_3). We calculated the charge transfer between Ti_{SI} and adjacent Ti_1, Ti_2, and Ti_3 atoms by the Bader analysis.[77] Ti_{SI}, Ti_1, Ti_2, and Ti_3 atoms lost 1.31, 0.88, 1.29, and 0.95 e electrons, while S_1, S_2, and S_3 atoms gained 2.98, 3.02, and 2.73 e electrons, as shown in Figure 3b. This redistribution of charge confirms that the Ti_{SI} atom leads to the observed magnetic properties, shown in Figure 2a−f. The introduced MM primarily arises from the Ti_{SI} atom and mainly localized the Ti_{SI} and nearby Ti_1, Ti_2, and Ti_3 atoms, shown in Figure 2a−f. Similar phenomena also appear in SI-2H-MoS_2.[45]

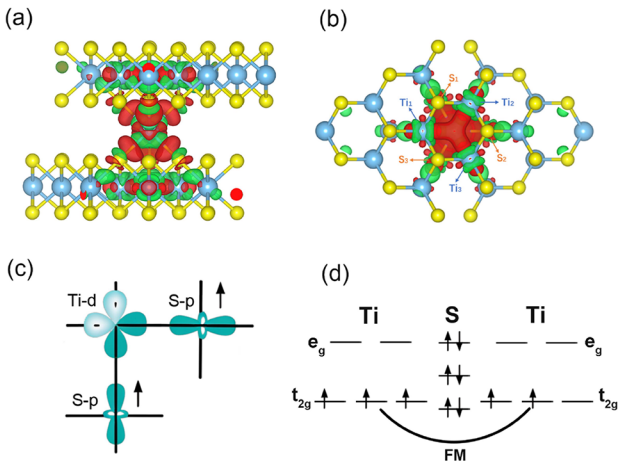

Figure 3. (a) Top and (b) side views of the differential charge density of $Ti_{19}S_{36}$. The red and green dots represent the accumulation and depletion of electrons, respectively. (c) Schematic of the superexchange mechanism for Ti_mS_n. (d) Schematic of the double-exchange mechanism among Ti_1, Ti_2, and Ti_3.

By combining Bader analysis, we propose several mechanisms responsible for FM coupling in Ti_mS_n. The Ti−S−Ti_{SI} bond angle is 95.27°, in accordance with the Goodenough−Kanamori−Anderson rule.[78−80] The overlap between the half-occupied d-orbitals of Ti atoms and the p-orbitals of S atoms leads to a relatively weak FM superexchange interaction, which results in the interlayer FM order (Figure 3c). Furthermore, the FM coupling between Ti_1, Ti_2, and Ti_3 atoms can be explained by the double-exchange mechanism, shown in Figure 3d. Due to the d-orbital occupation of Ti atoms in the layer being different, electrons can hop between them via the S atoms. In this process, one of the Ti atoms receives minority spin carriers from the S atom, while another Ti atom donates electrons to fill the vacant orbitals of the S atom. When these two Ti atoms are FM coupling, the carriers do not need to flip spin orientation, which creates a lower energy state. To sum up, Ti_{SI} introduces local charge doping and redistribution, directly changes the exchange mechanism, and causes FM coupling between Ti atoms.

https://doi.org/10.1021/acs.jpcc.4c06216
J. Phys. Chem. C XXXX, XXX, XXX−XXX

Electronic Properties. After investigating the magnetic configurations, the $Ti_{19}S_{36}$ showed an FM order, as shown in Figure 2a. The corresponding electronic band structure and DOS of $Ti_{19}S_{36}$ with the FM order were calculated, as depicted in Figure 4a. The valence band maximum (VBM) of $Ti_{19}S_{36}$ is

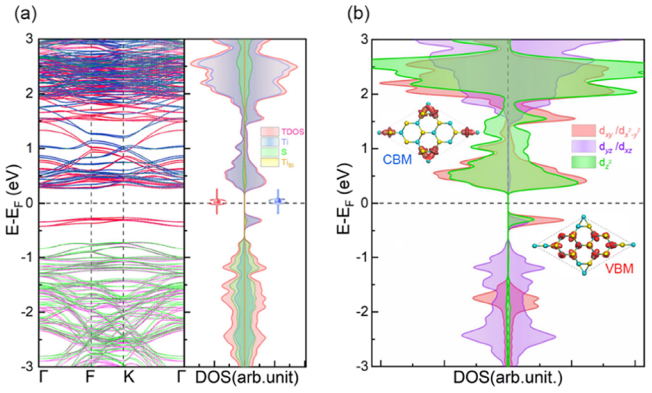

Figure 4. (a) Band structures and DOS of $Ti_{19}S_{36}$-AB stacking with FM order. The blue, red, green, and pink lines present Ti and S-projected band structure and PDOS. (b) Ti's *d*-orbital PDOS. The insets are the charge densities of CBM and VBM. The Fermi level is set at 0 eV.

contributed by the spin-α electrons, while the conduction band minimum (CBM) is contributed by the spin-β electrons, as shown in Figure 4b. Therefore, $Ti_{19}S_{36}$ is a BMS with a direct band gap of 0.53 eV, as shown in Figure 4a. The states of −0.5 eV below the Fermi level are primarily contributed by S atoms, while those above 0.5 eV are mainly contributed by Ti atoms. Specifically, the states within ±0.5 eV near the Fermi level are predominantly contributed by Ti atoms, consistent with the projected band structure, shown in Figure 4a. To further analyze the specific contribution of Ti atomic *d* orbitals, we plotted five *d* orbitals projected partial DOS (PDOS) and the charge densities of CBM and VBM, as shown in the inset of Figure 4b. Regardless of the CBM or VBM, d_{xy} and $d_{x^2-y^2}$ orbitals contribute the most, followed by the d_{z^2} orbital. However, the d_{yz} and d_{xz} orbitals make the least contribution. The charge density of the CBM is primarily from Ti_{SI} and the surrounding six-layer Ti atoms, while the charge density of the VBM comes from the remaining Ti atoms in the layers, consistent with the electronic structure analysis. Additionally, the d_{xy} and $d_{x^2-y^2}$ orbitals are degenerate. d_{yz} and d_{xz} orbitals are also degenerate. Both TiS_2-ML and multilayer are spin-unpolarized narrow-band-gap semiconductors.[81] Our calculation shows that the Ti_{SI} atom introduces spin-polarization.

Since the Ti atom is TM, the effect of SOC should be considered. We also calculated the band structures with EA along the [100] and [001] directions, respectively. After considering SOC, the $Ti_{19}S_{36}$ remains a semiconductor with a band gap of 0.55 eV. However, there is a splitting in the bands at Γ, F, and K points. More details can be found in Figure S2.

Dynamic and Thermodynamic Stability. The thermodynamic stability of $Ti_{19}S_{36}$ was assessed through phonon spectra and phonon DOS, as depicted in Figure 5a. The phonon spectra and their phonon DOS of Ti_9S_{16} (25%), $Ti_{15}S_{28}$ (14.3%), and $Ti_{19}S_{36}$ (11.1%) exhibit no imaginary frequency, indicating the thermodynamic stability of Ti_9S_{16} and $Ti_{15}S_{28}$. Additionally, the phonon spectra of the TiS_2 BL structure were calculated, as shown in Figure S3. The result

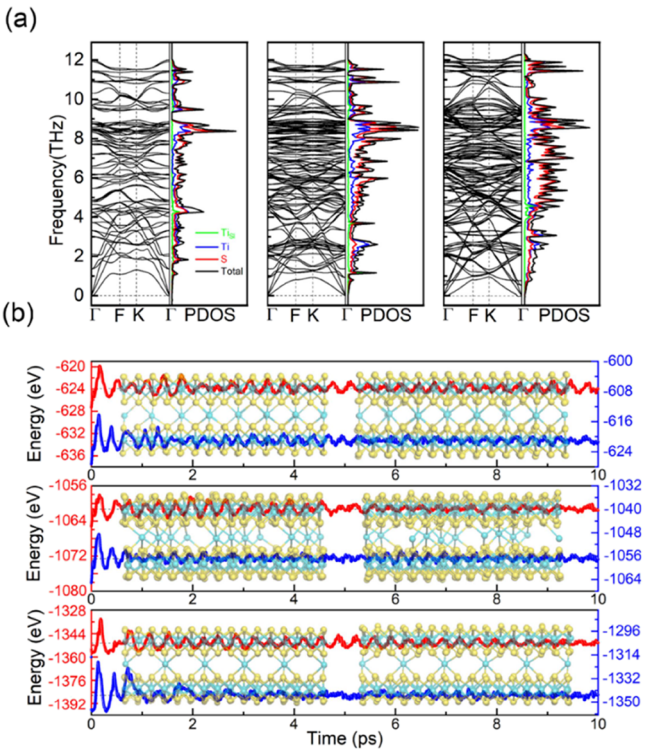

Figure 5. (a) Phonon band and phonon DOS of Ti_9S_{16} (25%), $Ti_{15}S_{28}$ (14.3%), and $Ti_{19}S_{36}$ (11.1%). The green, blue, red, and black lines represent Ti_{SI}, Ti, S, and total phonon DOS, respectively. (b) Functions of energies of Ti_9S_{16}, $Ti_{15}S_{28}$, and $Ti_{19}S_{36}$ in the simulation, from the top to the bottom. The red and blue lines represent simulated temperatures of 300 and 500 K, respectively.

reveals that the highest frequency for both TiS_2 BL and $Ti_{19}S_{36}$ (11.1%) is 12.3 THz, while the highest frequencies of Ti_9S_{16} (25%) and $Ti_{15}S_{28}$ (14.3%) are 12 THz. The highest frequency of the phonon spectra decreases as the number of Ti_{SI} atoms increases. It indicates that the Ti_{SI} atom restricts the system's vibration. The phonon DOS reveals that Ti atoms contribute to the low frequency (0−6 THz), whereas S atoms make more contribution to the high frequency (6−12 THz). It is related to the atomic mass of Ti (47.87) and S (32.07) atoms, respectively.

The thermal stability of 2H−SI−TiS_2 is evaluated with phonon spectra. We also perform AIMD simulations at 300 and 500 K to examine the geometrical stability, shown in Figure 5b. Ti_9S_{16}, $Ti_{15}S_{28}$, and $Ti_{19}S_{36}$ are performed by AIMD simulation to verify the dynamic stability. The average energies for Ti_9S_{16}, $Ti_{15}S_{28}$, and $Ti_{19}S_{36}$ are −623.9 (−621.1), −1060.3 (−1056.9), and −1350.4 (−1344.8) eV, at 300 and 500 K, as shown in Figure 5b. The average energy fluctuations per atom of Ti_9S_{16}, $Ti_{15}S_{28}$, and $Ti_{19}S_{36}$ at 300 K are 20, 21, and 24 meV, respectively. The average energy fluctuations per atom of Ti_9S_{16}, $Ti_{15}S_{28}$, and $Ti_{19}S_{36}$ at 500 K are 0.028, 0.038, and 0.042 eV, respectively. Random snapshots of the geometry during the simulation also prove the structural integrity, as shown in the inset of Figure 5b. In addition, the AIMD simulations of Ti_7S_{12} and $Ti_{20}S_{36}$ are also performed, shown in Figure S4. It demonstrates the dynamic stability of 2H−SI−TiS_2.

Magnetic Anisotropy Properties. MAE refers to the energy difference between the MM along the easy axis of magnetization (EA) and the hard axis. A larger MAE indicates

https://doi.org/10.1021/acs.jpcc.4c06216
J. Phys. Chem. C XXXX, XXX, XXX−XXX

it is difficult to change the direction of the magnetic axis. Generally, the MAE contains the magnetic shape anisotropy (MSA) energy, E_{MSA}, and the magnetocrystalline anisotropy (MCA) energy, EMCA, which are mainly contributed by the dipole−dipole interaction and the spin−orbit coupling effect, respectively. The E_{MSA} can be calculated by the following equation:

$$E_{MSA} = E_{Dipole[100]} - E_{Dipole[001]} \tag{9}$$

where $E_{Diople[100]}$ and $E_{Diople[001]}$ represent the energies of the magnetic dipole−dipole interaction with EA along the [100] and [001] directions, respectively. They can be obtained by the following equation:

$$E_{Dipole} = -\frac{1}{2}\frac{\mu_0}{4\pi}\sum_{i\neq j}^{n}\frac{1}{r_{ij}^3}\left[M_i\cdot M_j - \frac{3}{r_{ij}^2}\left(M_i\cdot r_{ij}\right)\left(M_j\cdot r_{ij}\right)\right] \tag{10}$$

where M_i and M_j are the local MMs, and r_{ij} is the vector from site i to j. The E_{MSA} values of $Ti_{19}S_{36}$ (11.1%) and $Ti_{33}S_{64}$ (6.25%) are 1.67×10^{-2} and 1.74×10^{-2} meV. Given that the primary contributors to MSA are the Ti_{SI} and their neighboring Ti atoms, the MM and the r_{ij} remain largely invariant across structures with varying x. Consequently, the impact of MSA on x is comparatively minimal.

In the MCA section, we used the LDA+U method to calculate the concentrations of $Ti_{19}S_{36}$ and $Ti_{33}S_{64}$. We test the k point before calculating the MCA, as shown in Figure S5. The polar angle (θ) and the azimuthal angle of the magnetization axis (ϕ) are presented in Figure 6a. 2H−SI−

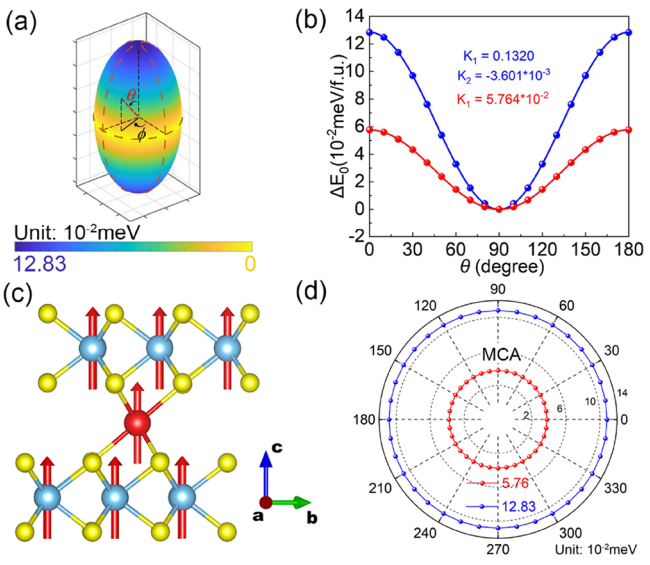

Figure 6. (a) The ΔE_0 for $Ti_{33}S_{64}$ (6.25%) with an x of 50% changes with θ and ϕ. (b) The ΔE_0 of $Ti_{19}S_{36}$ (11.11%) and $Ti_{33}S_{64}$ (6.25%) with AB stacking changes with θ. (c) The EA is along the [001] direction. (d) The ΔE_0 of $Ti_{19}S_{36}$ and $Ti_{33}S_{64}$ changes with ϕ. The red and blue lines represent $Ti_{19}S_{36}$ and $Ti_{33}S_{64}$, respectively.

TiS_2 belongs to the hexagonal lattice, and the relationship between energy and θ, ϕ can be expressed by the following equations:

$$\Delta E_0 = K_1\cos^2\theta + K_2\cos^4\theta + K_3\cos^6\theta + K_4\cos 3\phi \tag{11}$$

$$\Delta E_0 = E - E_{[001]} \tag{12}$$

where K_1, K_2, and K_3 represent the quadratic, quartic, and sextic contributions to the MCA, respectively. ΔE_0 is independent of the in-plane azimuthal angle ϕ, shown in Figure 6a, due to the high symmetry (D_{3d}). Therefore, K_4 equals 0.[82] It implies that ΔE_0 is the same for any in-plane direction of the magnetic axis. Therefore, the equation is simplified into

$$\Delta E_0 = K_1\cos^2\theta + K_2\cos^4\theta + K_3\cos^6\theta \tag{13}$$

ΔE_0 of $Ti_{19}S_{36}$ satisfies the following equation:

$$\Delta E_0\ (10^{-2}\ \text{meV}) = 5.763 \times 10^{-2}\cos^2\theta - 2.615 \times 10^{-6}\cos^4\theta + 2.661 \times 10^{-5}\cos^6\theta \tag{14}$$

Since K_1 is much larger than K_2 and K_3, we use ΔE_0 (10^{-2} meV) = $5.764 \times 10^{-2}\cos^2\theta$ to fit the curve. Additionally, the ΔE_0 of $Ti_{33}S_{64}$ satisfies the following equation:

$$\Delta E_0\ (10^{-2}\ \text{meV}) = 0.1320\cos^2\theta - 3.601 \times 10^{-3}\cos^4\theta \tag{15}$$

When $\theta = \frac{\pi}{2}$, ΔE_0 has the lowest value; when $\theta = 0$ or $\theta = \pi$, ΔE_0 has the highest value, shown in Figure 6b. EA is out-of-plane, which corresponds to the PMA, shown in Figure 6c. The MCA can be calculated by the following equation[70]:

$$\text{MCA} = E_{[100]} - E_{[001]} \tag{16}$$

where $E_{[100]}$ and $E_{[001]}$ represent the energies with EA along the [100] and [001] directions, respectively. The MCAs of $Ti_{19}S_{36}$ and $Ti_{33}S_{64}$ are 5.76×10^{-2} and 12.83×10^{-2} meV, indicating that EA points to the out-of-plane direction, resulting in PMA, as shown in Figure 6d.

In summary, the EMAEs of $Ti_{19}S_{36}$ and $Ti_{33}S_{64}$ are 7.43×10^{-2} and 14.57×10^{-2} meV, respectively. Averaging out per Ti atom, they are 0.391 and 0.442 meV/Ti, respectively.

Atom-Orbital-Resolved MCA. In order to explain the different MCAs of $Ti_{19}S_{36}$ and $Ti_{33}S_{64}$, it is necessary to elucidate the contribution of atomic orbitals to the MCA. Tight-binding and second-order perturbation theory[45,48,83] are used. The MCA of each atom (MCA_i) can be assessed using the canonical formulation equation:

$$\text{MCA}_i = \left[\int E_f(E - E_F)[n_i^{[100]}(E) - n_i^{[001]}(E)]\right] \tag{17}$$

where MCA_i represents the ith atom's MCA. $n_i^{[100]}(E)$ and $n_i^{[001]}(E)$ are the DOS of the ith atom with EA along the [100] and [001] directions, respectively. The Ti_mS_n with AB stacking has a D_{3d} group. As a result, the energies with EA along [010] ($E_{[010]}$) and [100] ($E_{[100]}$) are the same. Therefore, only $E_{[100]}$ is calculated. Furthermore, the total MCA could be obtained as the sum of MCA_i. Based on the second-order perturbation theory, MCA can be obtained by the following terms[45,48,83]:

$$\Delta E^{--} = E_x^{--} - E_z^{--} = \xi^2 \sum_{o^+,u^-} \left(|\langle o^-|L_z|u^-\rangle|^2 - |\langle o^-|L_x|u^-\rangle|^2\right) / (E_u^- - E_o^-) \tag{18}$$

https://doi.org/10.1021/acs.jpcc.4c06216
J. Phys. Chem. C XXXX, XXX, XXX−XXX

Table 1. Matrix Differences for d Orbitals between Magnetization along the [001] and [100] Directions in Eqs 18 and 19

	o^+					o^-				
u^-	d_{xy}	d_{yz}	d_{z^2}	d_{xz}	$d_{x^2-y^2}$	d_{xy}	d_{yz}	d_{z^2}	d_{xz}	$d_{x^2-y^2}$
d_{xy}	0	0	0	1	−4	0	0	0	−1	4
d_{yz}	0	0	3	−1	1	0	0	−3	1	−1
d_{z^2}	0	3	0	0	0	0	−3	0	0	0
d_{xz}	1	−1	0	0	0	−1	1	0	0	0
$d_{x^2-y^2}$	−4	1	0	0	0	4	−1	0	0	0

$$\Delta E^{-+} = E_x^{+-} - E_z^{+-} = \xi^2 \sum_{o^+,u^-} (|\langle o^+|L_z|u^-\rangle|^2 - |\langle o^+|L_x|u^-\rangle|^2) / (E_u^- - E_o^-) \quad (19)$$

where + and − represent spin-α and spin-β electrons, and ξ, L_x, and L_z are the SOC constants, associated with the angular momentum operators along the [100] and [001] directions, respectively. u and o represent unoccupied and occupied states, and E_o and E_u are the energies of occupied and unoccupied states, respectively.

MCA primarily arises from the contribution of spin−orbital matrix elements and energy differences. MCA is related to the intensity of DOS near the Fermi level. Apart from that, the matrix element differences $|\langle o^-|L_z|u^-\rangle|^2 - |\langle o^-|L_x|u^-\rangle|^2$ and $|\langle o^+|L_z|u^-\rangle|^2 - |\langle o^+|L_x|u^-\rangle|^2$ for d and p orbitals are calculated, shown in Tables 1 and 2, respectively.

Table 2. Matrix Differences for p Orbitals between EA along the [001] and [100] Directions in Eqs 18 and 19

	o^+			o^-		
u^-	p_y	p_z	p_x	p_y	p_z	p_x
p_y	0	1	−1	0	−1	1
p_z	1	0	0	−1	0	0
p_x	−1	0	0	1	0	0

To further elucidate the variation of MCA, the atom-orbital-resolved MCA is depicted in Figure 7. The total MCA of $Ti_{19}S_{36}$ (11.11%) is 57.6 μeV. S atoms contribute 7.60 μeV, while Ti_{BL} and Ti_{SI} atoms contribute 40.6 and 8.80 μeV, respectively. Atomic hybridization of $Ti_{19}S_{36}$ between occupied $d_{x^2-y^2}$ and unoccupied d_{xy} orbitals of the Ti_{BL}'s atom contributes to PMA (39.0 μeV), which corresponds to matrix difference 4 for d orbitals, shown in Figure 7a and Table 1. In addition, the atomic hybridization between Ti_{SI}'s $d_{x^2-y^2}$ and d_{xy} orbitals contributes to PMA (23.6 μeV), which corresponds to the matrix difference 4, shown in Figure 7b and Table 1. In addition, the atomic hybridization between S's p_x and p_y orbitals, which corresponds to the matrix difference 1, is shown in Figure 7c and Table 2. The total MCA of $Ti_{33}S_{64}$ (6.25%) is 128.3 μeV. S atoms contribute 21.6 μeV, while Ti_{BL} and Ti_{SI} atoms contribute 70.9 and 9.30 μeV, respectively.

By comparing the MCA and orbital interaction in both cases, it can be found that when x decreases, the hybridization interaction between the $d_{x^2-y^2}$ and d_{xy} orbitals of Ti_{BL} becomes stronger. The hybridization interaction between the p_x and p_y orbitals of S becomes stronger. However, the hybridization interaction between the $d_{x^2-y^2}$ and d_{xy} orbitals of the Ti_{SI} atom becomes weaker. Overall, the MCA gets larger as x decreases.

NEB Transition State Search. To investigate the stability of 2H−SI−TiS_2, we performed a transition state search of $Ti_{19}S_{36}$ between the adjacent coordination sites of the intercalated atoms. The energy barrier for this transition was calculated using the CI-NEB method.[48,74] Six images were

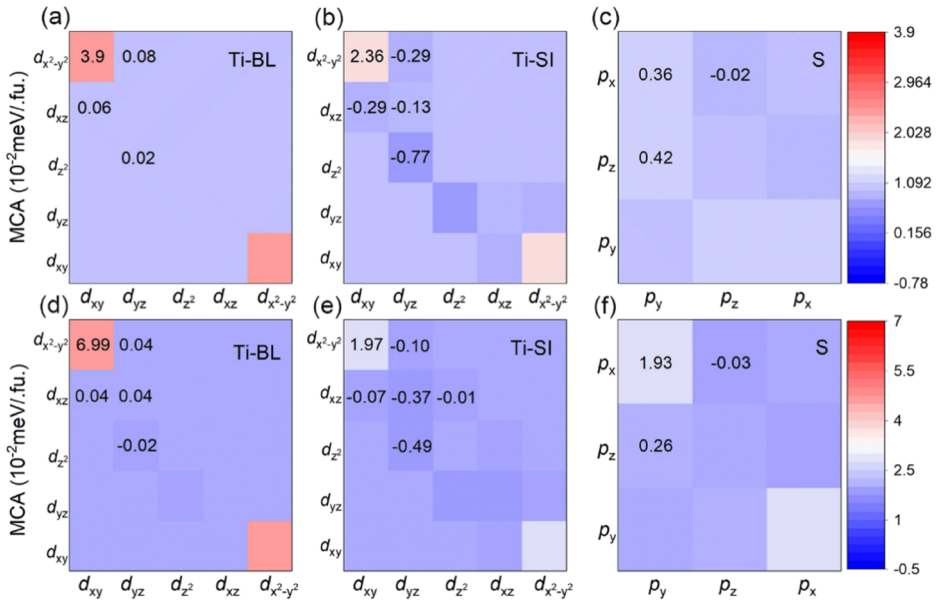

Figure 7. Orbital-resolved MCA of $Ti_{19}S_{36}$ (a−c) and $Ti_{33}S_{64}$ (d−f). Orbital-resolved (a) Ti_{BL}, (b) Ti_{SI}, and (c) S orbital-resolved MCA of $Ti_{19}S_{36}$. Orbital-resolved (d) Ti_{BL}, (e) Ti_{SI}, and (f) S orbital-resolved MCA of $Ti_{33}S_{64}$.

https://doi.org/10.1021/acs.jpcc.4c06216
J. Phys. Chem. C XXXX, XXX, XXX−XXX

inserted, and the energy difference of eight structures was calculated, as illustrated in Figure 8. When the Ti_{SI} atom moves

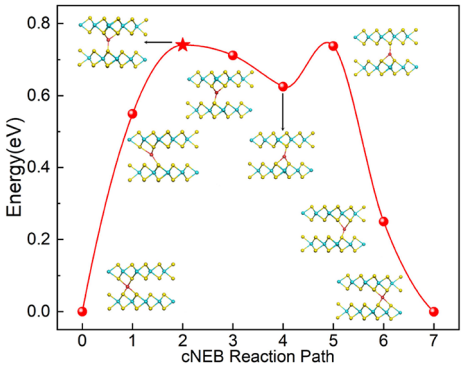

Figure 8. Energies as a function of the reaction ordinate. The side view of every path's structure is shown in the inset.

from the hollow site to the position above an S atom of the lower layer, the energy reaches its highest value, as shown in the inset of Figure 8. The energy then decreases over the next two steps. When the Ti_{SI} atom moves to a position below an S atom of the upper layer, the energy peaks again before it drops. This behavior indicates that the energy barrier is higher due to spatial hindrance, as the distance between the two layers is difficult to change after the intercalated structure is formed.

In the geometry of the transition state, the distance between Ti_{SI} and the S atom below it is 2.423 Å, and three S atoms above it have a bond length of 2.436 Å, as shown in Figure S6. The calculated migration energy barrier for Ti_{SI} between adjacent hollow sites is 0.740 eV, indicating that the Ti_{SI} atom is difficult to migrate. This high energy barrier demonstrates that Ti_{SI} is difficult to move between different sites.

Formation Energy Analysis. In order to verify the synthesis feasibility of Ti_mS_n, the formation energy is calculated. ε_f refers to the energy needed when a compound is formed from its constituent elements. For Ti_mS_n, ε_f can be calculated using the chemical composition and the total energy of the system. The ε_f of TiS_2 is given by

$$\varepsilon_f = E_{total} - m \times \mu_{Ti} - n \times \mu_S \quad (20)$$

$$\mu_{Ti} + 2\mu_S = \varepsilon_{TiS_2} \quad (21)$$

where E_{total} and ε_{TiS_2} represent the total energy and the energy of the supercell, respectively. μ_{Ti} and μ_S represent the chemical potentials of the Ti and S atoms, respectively. m and n are the numbers of Ti and S atoms in Ti_mS_n. By modifying the above equation, we obtain

$$\begin{aligned}\varepsilon_f &= E_{total} - m \times \mu_{Ti} - n \times \mu_S \\ &= E_{total} - m \times (\varepsilon_{TiS_2} - 2\mu_S) - n \times \mu_S \\ &= E_{total} - m \times \varepsilon_{TiS_2} + (2m - n) \times \mu_S \end{aligned} \quad (22)$$

$$\varepsilon = \varepsilon_f/[(m-1)/2] = 2\varepsilon_f/(m-1) \quad (23)$$

ε_{TiS_2} was calculated to be −16.445 eV. The ε_f of 2H−SI−TiS_2 as a function of μ_S, which ranges from 2.4 eV below μ_{S_8bulk} to 1.6 eV above μ_{S_8bulk}, was calculated. We also considered the impact of x ($2.8\% < \varepsilon < 100\%$) on ε_f, as shown in Figure 9a. In order to evaluate the change of ε_f with different x, we first optimized the geometries of 2H−SI−TiS_2, shown in Figure S7.

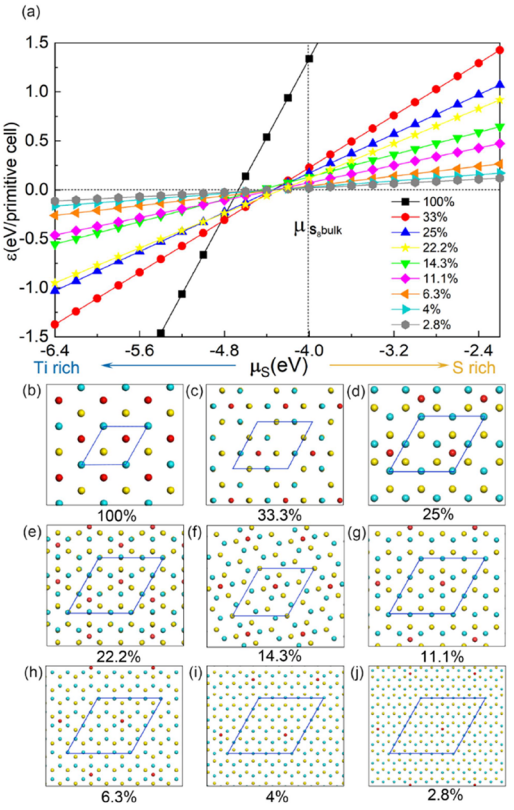

Figure 9. (a) ε_f as a function of μ_S. The gray, cyan, orange, pink, green, yellow, blue, red, and black dots represent x values of 2.8, 4, 6.3, 11.1, 14.3, 22.2, 25, 33, and 100%, respectively. Top view of Ti_mS_n with x of (b) 100%, (c) 33.3%, (d) 25%, (e) 22.2%, (f) 14.3%, (g) 11.1%, (h) 6.3%, (i) 4%, and (j) 2.8%.

The corresponding geometries of 100, 33.3, 25, 22.2, 14.3, 11.1, 6.3, 4, and 2.8% are shown in Figure 9b−j, respectively. Taking $Ti_{19}S_{36}$ (11%) as an example, the ε_f values are −0.461, −0.283, −0.106, 0.072, 0.250, and 0.428 eV per unit cell, when μ_S values are −6.4, −5.6, −4.8, −4.0, −3.2, and −2.4 eV, shown as the pink line with the diamond in Figure 9a. When the μ_S is higher than −4.3 eV (low μ_{Ti}), the higher x results in larger ε_f (shown in Figure 9a), which means that the synthesis tends to favor Ti_mS_n with a lower x. For instance, the ε_f values are 2.938 (100%), 0.759 (33%), 0.571 (25%), 0.473 (22.2%), 0.360 (14.3%), 0.250 (11.1%), 0.139 (6.3%), 0.091 (4%), and 0.064 eV (2.8%) per unit cell, at the μ_S of −3.2 eV. Conversely, when the μ_S is lower than −4.3 eV (high μ_{Ti}), a higher x of synthesized Ti_mS_n leads to a lower ε_f. This indicates that the synthesis tends to favor Ti_mS_n with a higher x. For example, the ε_f values are −1.862 (100%), −0.841 (33%), −0.629 (25%), −0.593 (22.2%), −0.326 (14.3%), −0.283 (11.1%), −0.161 (6.3%), −0.101 (4%), and −0.070 eV (2.8%) per unit cell, at the μ_S of −5.6 eV. Therefore, it can be found that stoichiometric 2H-TiS_2 is formed only under the S-rich condition (when the μ_S exceeds −4.3 eV). 2H−SI−TiS_2 is likely to be synthesized in a Ti-rich environment. When the Ti:S flux ratio is higher (lower μ_S), SI structures with x ($2.8\% < x < 33\%$) can be easily synthesized.

In the synthesis, the insertion process of Ti is further promoted due to the volatilization of S.[60] This calculation suggests that the synthesis is energetically feasible, and MBE[84] or chemical vapor deposition (CVD)[85] could be used to synthesize 2H−SI−TiS_2.

https://doi.org/10.1021/acs.jpcc.4c06216
J. Phys. Chem. C XXXX, XXX, XXX−XXX

Magnetic Properties with *x*. In order to explore the regulation of Ti_mS_n properties at different concentrations, we tested four magnetic orders for the structures of each *x*, and the corresponding energies can be found in Figure S8. When *x* is 100 and 33%, the corresponding Ti_mS_n shows an AFM order. When *x* is 25 and 14.3%, Ti_mS_n shows the ferrimagnetic(FiM)-1 order. As *x* is decreased to 11.1, 6.3, and 4%, the Ti_mS_n becomes an FM order, with an energy of about 70 meV lower than the other three states, shown in Figure S8. More details can be found in the Supporting Information. Therefore, we conclude that Ti_mS_n shows an FM order when the Ti_mS_n value of *x* is less than 11.11%.

Electronic Properties with *x*. Besides the electronic structure of $Ti_{19}S_{36}$ (11.11%), we also calculated the electronic structures of Ti_mS_n with *x* values of 2.8, 4, 6.3, 14.3, 22.2, 25, 33, and 100%, shown in Figure 10a. The Ti_mS_n with *x* of 2.8%,

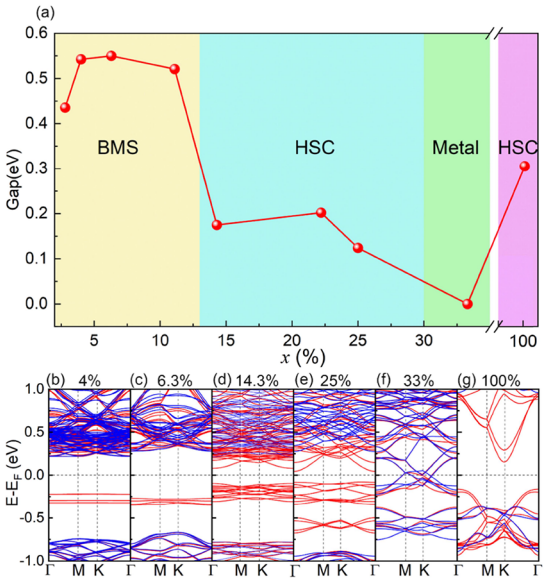

Figure 10. (a) Gap energy changes with *x*. Band structures of (b) $Ti_{51}S_{100}$ (4%), (c) $Ti_{33}S_{64}$ (6.3%), (d) $Ti_{15}S_{28}$ (14.3%), (e) Ti_9S_{16} (25%), (f) Ti_7S_{12} (33%), and (g) Ti_3S_4 (100%).

4% (Figure 10b), 6.3% (Figure 10c), and 11.1% are BMS with band gaps of 0.436, 0.543, 0.550, and 0.521 eV. As *x* is increased to 14.3, 22.2, and 25%, Ti_mS_n translates into HSC with gaps of 0.175, 0.202, and 0.124 eV, respectively. Ti_7S_{12} (33%) becomes a spin-polarized metal, as shown in Figure 10f. Interestingly, Ti_3S_4 reverts to an HSC with a gap of 0.305 eV, as shown in Figure 10g, when *x* reaches 100%.

The *x* significantly influences the electronic structure of 2H−SI−TiS_2. The band structures with increasing *x* from left to right are shown in Figure 10b−g. TiS_2 BL is a nonpolarized semiconductor with an indirect gap of 1.00 eV, shown in Figure S9. The insertion of the Ti_{SI} atom introduces new electronic states around −0.25 eV, resulting in a smaller gap. As *x* is increased to 14.3%, the sub-bands of spin-α electrons below the Fermi level rise, and the sub-bands of spin-α electrons above the Fermi level drop, as shown in Figure 10d. This results in a reduced band gap, and Ti_mS_n transforms from a semiconductor into an HSC. As *x* grows to 33.3%, spin-α and spin-β electrons of Ti_7S_{12} come across the Fermi level, rendering the Ti_7S_{12} metallic. When *x* is further increased to 100%, Ti_3S_4 becomes an HSC again.

Additionally, we investigated the effect of the number of stacked layers on the magnetic order and band structure of SI-TiS_2-AB stacking. We constructed self-intercalated structures with three, four, and five TiS_2 layers, ensuring that Ti_{SI} atoms in different layers occupy the same horizontal position, as shown in Figure S10. The magnetic orders of the three structures are shown in Figure S10. The three-layer SI-TiS_2 becomes a spin-polarized metal, while the four-layer and five-layer SI-TiS_2 revert to HSC. The details can be found in Figure S11. The result shows that we can achieve a range of electronic properties, from BMS to HSC and spin-polarized metals, by varying the *x* or the number of layers.

CONCLUSIONS

In summary, the magnetic and electronic properties of 2H−SI−TiS_2 with AB stacking are systematically investigated. We reveal that the Ti_{SI} atom can introduce a long-range magnetic order to nonmagnetic 2H-TiS_2 BL. When *x* is below 11.1%, 2H−SI−TiS_2 is BMS with an FM order. $Ti_{19}S_{36}$ (11.1%) is used to study the magnetic exchange mechanism and estimate the T_C to be 377 K. Besides, $Ti_{19}S_{36}$ tends to PMA with an MAE of 7.43×10^{-2} meV. MAE decreases as *x* increases because the hybridization interaction between $d_{x^2-y^2}$ and d_{xy} orbitals of Ti_{BL} becomes weaker. Meanwhile, Ti_mS_n undergoes a transition from BMS to HSC and the metal. Ti_mS_n shows good thermodynamic and dynamic stabilities at 300 and 500 K, respectively. The ε_f value of Ti_mS_n is related to both *x* and μ. Ti_mS_n with Ti_{SI} atoms are more easily synthesized under a higher μ_{Ti}. The migration barrier of 0.740 eV proves that Ti_{SI} is difficult to transfer between adjacent hollow sites after the formation of $Ti_{19}S_{36}$. Our findings reveal an FM material and demonstrate the potential of nonmagnetic materials as candidate materials for spintronic quantum.

ASSOCIATED CONTENT

Supporting Information

The Supporting Information is available free of charge at https://pubs.acs.org/doi/10.1021/acs.jpcc.4c06216.

Atomic displacement after SI, details of Monte Carlo simulation, band structure with SOC, phonon of TiS_2-AB BL, K-mesh test, CI-NEB search, geometries of 2H−SI−TiS_2 with *x*, ΔE of different magnetic orders in Ti_mS_n, electronic structure of TiS_2−BL, geometries and band structures of the 2H−SI−TiS_2 multilayer, and detailed structural information (PDF)

AUTHOR INFORMATION

Corresponding Author

Zhaoyong Guan − *Key Laboratory of Colloid and Interface Chemistry, Ministry of Education, School of Chemistry and Chemical Engineering and School of Chemistry and Chemical Engineering, Shandong University, Jinan, Shandong 250100, P. R. China;* orcid.org/0000-0002-6847-5809; Phone: +86-0531-88363179; Email: zyguan@sdu.edu.cn; Fax: +86-0531-88363179

Authors

Fangyu Zhang − *Key Laboratory of Colloid and Interface Chemistry, Ministry of Education, School of Chemistry and Chemical Engineering and School of Chemistry and Chemical Engineering, Shandong University, Jinan, Shandong 250100, P. R. China*

https://doi.org/10.1021/acs.jpcc.4c06216
J. Phys. Chem. C XXXX, XXX, XXX−XXX

Linhui Lv − *Key Laboratory of Colloid and Interface Chemistry, Ministry of Education, School of Chemistry and Chemical Engineering and School of Chemistry and Chemical Engineering, Shandong University, Jinan, Shandong 250100, P. R. China;* orcid.org/0009-0008-6594-5116

Zihao Xu − *School of Physics, Shandong University, Jinan, Shandong 250100, P. R. China*

Diancong Qi − *Key Laboratory of Colloid and Interface Chemistry, Ministry of Education, School of Chemistry and Chemical Engineering and School of Chemistry and Chemical Engineering, Shandong University, Jinan, Shandong 250100, P. R. China*

Weiyi Wang − *Department of Chemical Physics and Hefei National Laboratory for Physical Sciences at Microscale, University of Science and Technology of China, Hefei, Anhui 230026, China;* orcid.org/0000-0001-6981-2611

Xingxing Li − *Department of Chemical Physics and Hefei National Laboratory for Physical Sciences at Microscale, University of Science and Technology of China, Hefei, Anhui 230026, China;* orcid.org/0000-0001-7820-0772

Ya Su − *School of Electrical Engineering, Shandong University, Jinan, Shandong 250100, P. R. China*

Yanyan Jiang − *Key Laboratory for Liquid−Solid Structural Evolution and Processing of Materials (Ministry of Education), School of Materials Science and Engineering, Shandong University, Jinan, Shandong 250061, People's Republic of China;* orcid.org/0000-0002-7866-4689

Complete contact information is available at: https://pubs.acs.org/10.1021/acs.jpcc.4c06216

Notes

The authors declare no competing financial interest.

■ ACKNOWLEDGMENTS

The authors thank Prof. Wenhui Duan for the discussion of the evaluation of T_C, Prof. Bin Wang for the discussion of magnetic properties, Prof. Wen Zhao for the discussion of the evaluation of formation energy, and Prof. Wei Wei for the discussion of the analysis of magnetic exchanged parameters, the MCA calculation, and the LDA+U method. This work was supported financially by the Natural Science Foundation of China (Grant No. 11904203), the Fundamental Research Funds of Shandong University (Grant No. 2019GN065), and the Natural Science Foundation of Shandong Province (ZR2023MA019). Dr. Weiyi Wang acknowledges the Postdoctoral Fellowship Program of China Postdoctoral Science Foundation (No. GZC20232540). The computational resources were from the Shanghai Supercomputer Center. The scientific calculations in this paper were performed on the HPC Cloud Platform of Shandong University. The authors are grateful to Beijing Beilong Super Cloud Computing Co., Ltd for the computation resource in the Beijing Super Cloud Computing Center. The numerical calculations in this paper were done at the Hefei Advanced Computing Center.

■ REFERENCES

(1) Butler, S. Z.; Hollen, S. M.; Cao, L.; Cui, Y.; Gupta, J. A.; Gutiérrez, H. R.; Heinz, T. F.; Hong, S. S.; Huang, J.; Ismach, A. F.; et al. Progress, Challenges, and Opportunities in Two-Dimensional Materials Beyond Graphene. *ACS Nano* **2013**, *7* (4), 2898−2926.

(2) Novoselov, K. S.; Geim, A. K.; Morozov, S. V.; Jiang, D.; Zhang, Y.; Dubonos, S. V.; Grigorieva, I. V.; Firsov, A. A. Electric Field Effect in Atomically Thin Carbon Films. *Science* **2004**, *306* (5696), 666−669.

(3) Huang, B.; Clark, G.; Navarro-Moratalla, E.; Klein, D. R.; Cheng, R.; Seyler, K. L.; Zhong, D.; Schmidgall, E.; McGuire, M. A.; Cobden, D. H.; et al. Layer-dependent ferromagnetism in a van der Waals crystal down to the monolayer limit. *Nature* **2017**, *546* (7657), 270−273.

(4) Zhao, Y.; Gu, J.; Chen, Z. Oxygen Evolution Reaction on 2D Ferromagnetic Fe_3GeTe_2: Boosting the Reactivity by the Self-Reduction of Surface Hydroxyl. *Adv. Funct. Mater.* **2019**, *29* (44), No. 1904782.

(5) Gong, C.; Li, L.; Li, Z.; Ji, H.; Stern, A.; Xia, Y.; Cao, T.; Bao, W.; Wang, C.; Wang, Y.; et al. Discovery of intrinsic ferromagnetism in two-dimensional van der Waals crystals. *Nature* **2017**, *546* (7657), 265−269.

(6) Kong, T.; Stolze, K.; Timmons, E. I.; Tao, J.; Ni, D.; Guo, S.; Yang, Z.; Prozorov, R.; Cava, R. J. VI_3—a New Layered Ferromagnetic Semiconductor. *Adv. Mater.* **2019**, *31* (17), No. 1808074.

(7) Jin, W.; Kim, H. H.; Ye, Z.; Li, S.; Rezaie, P.; Diaz, F.; Siddiq, S.; Wauer, E.; Yang, B.; Li, C.; et al. Raman fingerprint of two terahertz spin wave branches in a two-dimensional honeycomb Ising ferromagnet. *Nat. Commun.* **2018**, *9* (1), 5122.

(8) Yu, W.; Li, J.; Herng, T. S.; Wang, Z.; Zhao, X.; Chi, X.; Fu, W.; Abdelwahab, I.; Zhou, J.; Dan, J.; et al. Chemically Exfoliated VSe_2 Monolayers with Room-Temperature Ferromagnetism. *Adv. Mater.* **2019**, *31* (40), No. 1903779.

(9) Li, J.; Zhao, B.; Chen, P.; Wu, R.; Li, B.; Xia, Q.; Guo, G.; Luo, J.; Zang, K.; Zhang, Z.; et al. Synthesis of Ultrathin Metallic MTe_2 (M = V, Nb, Ta) Single-Crystalline Nanoplates. *Adv. Mater.* **2018**, *30* (36), No. 1801043.

(10) Frey, N. C.; Kumar, H.; Anasori, B.; Gogotsi, Y.; Shenoy, V. B. Tuning Noncollinear Spin Structure and Anisotropy in Ferromagnetic Nitride MXenes. *ACS Nano* **2018**, *12* (6), 6319−6325.

(11) Kargar, F.; Coleman, E. A.; Ghosh, S.; Lee, J.; Gomez, M. J.; Liu, Y.; Magana, A. S.; Barani, Z.; Mohammadzadeh, A.; Debnath, B.; et al. Phonon and Thermal Properties of Quasi-Two-Dimensional $FePS_3$ and $MnPS_3$ Antiferromagnetic Semiconductors. *ACS Nano* **2020**, *14* (2), 2424−2435.

(12) Han, W. Perspectives for spintronics in 2D materials. *APL Mater.* **2016**, *4* (3), No. 032401.

(13) Li, X.; Wu, X. Two-dimensional monolayer designs for spintronics applications. *WIREs Comput. Mol. Sci.* **2016**, *6* (4), 441−455.

(14) Wang, Q. H.; Kalantar-Zadeh, K.; Kis, A.; Coleman, J. N.; Strano, M. S. Electronics and optoelectronics of two-dimensional transition metal dichalcogenides. *Nat. Nanotechnol.* **2012**, *7* (11), 699−712.

(15) Mak, K. F.; Shan, J. Photonics and optoelectronics of 2D semiconductor transition metal dichalcogenides. *Nat. Photonics* **2016**, *10* (4), 216−226.

(16) Wu, Y.; Li, D.; Wu, C.-L.; Hwang, H. Y.; Cui, Y. Electrostatic gating and intercalation in 2D materials. *Nat. Rev. Mater.* **2023**, *8* (1), 41−53.

(17) Zhang, X.; Hou, L.; Ciesielski, A.; Samorì, P. 2D Materials Beyond Graphene for High-Performance Energy Storage Applications. *Adv. Energy Mater.* **2016**, *6* (23), No. 1600671.

(18) Gong, S.-J.; Gong, C.; Sun, Y.-Y.; Tong, W.-Y.; Duan, C.-G.; Chu, J.-H.; Zhang, X. Electrically induced 2D half-metallic antiferromagnets and spin field effect transistors. *Proc. Natl. Acad. Sci. U.S.A.* **2018**, *115* (34), 8511−8516.

(19) Ould-Mohamed, M.; Ouahrani, T.; Ougherb, C.; Franco, R.; Errandonea, D. Tuning the electronic properties of asymmetric YZrCOF MXene for water splitting applications: an ab initio study. *Dalton Trans.* **2024**, *53* (9), 4266−4277.

(20) Ould-Mohamed, M.; Ouahrani, T.; Boufatah, R.; Morales-García, Á.; Franco, R.; Badawi, M.; Errandonea, D. Janus $ScYCBr_2$ MXene as a Promising Thermoelectric Material. *ACS Appl. Energy Mater.* **2024**, *7* (15), 6598−6611.

(21) Wan, J.; Lacey, S. D.; Dai, J.; Bao, W.; Fuhrer, M. S.; Hu, L. Tuning two-dimensional nanomaterials by intercalation: materials, properties and applications. *Chem. Soc. Rev.* **2016**, *45* (24), 6742−6765.
(22) Rajapakse, M.; Karki, B.; Abu, U. O.; Pishgar, S.; Musa, M. R. K.; Riyadh, S. M. S.; Yu, M.; Sumanasekera, G.; Jasinski, J. B. Intercalation as a versatile tool for fabrication, property tuning, and phase transitions in 2D materials. *npj 2D Mater. Appl.* **2021**, *5* (1), 30.
(23) Stark, M. S.; Kuntz, K. L.; Martens, S. J.; Warren, S. C. Intercalation of Layered Materials from Bulk to 2D. *Adv. Mater.* **2019**, *31* (27), No. 1808213.
(24) Wu, Z.; Wu, Z.; Yu, J.; Yu, J.; Yuan, S.; Yuan, S. Strain-tunable magnetic and electronic properties of monolayer CrI_3. *Phys. Chem. Chem. Phys.* **2019**, *21* (15), 7750−7755.
(25) Yang, B.; Zhang, X.; Yang, H.; Han, X.; Yan, Y. Strain controlling transport properties of heterostructure composed of monolayer CrI_3. *Appl. Phys. Lett.* **2019**, *114* (19), 192405.
(26) Vishkayi, S. I.; Torbatian, Z.; Qaiumzadeh, A.; Asgari, R. Strain and electric-field control of spin-spin interactions in monolayer CrI_3. *Phys. Rev. Mater.* **2020**, *4* (9), No. 094004.
(27) Kong, X.; Kong, X.; Yoon, H.; Yoon, H.; Han, M. J.; Han, M. J.; Liang, L.; Liang, L. Switching interlayer magnetic order in bilayer CrI_3 by stacking reversal. *Nanoscale* **2021**, *13* (38), 16172−16181.
(28) Li, S.; Hou, Y.; Zhou, M.; Li, M.; Zheng, F.; Shao, X.; Zhang, P. Stacking order, charge doping, and strain-induced switching between AFM and FM in bilayer GdI_2. *J. Appl. Phys.* **2023**, *134* (12), 123901.
(29) Sun, Y.-Y.; Zhu, L.-Q.; Li, Z.; Ju, W.; Gong, S.-J.; Wang, J.-Q.; Chu, J.-H. Electric manipulation of magnetism in bilayer van der Waals magnets. *J. Phys.: Condens. Matter* **2019**, *31* (20), 205501.
(30) Jiang, S.; Shan, J.; Mak, K. F.; Jiang, S.; Shan, J.; Mak, K. F. Electric-field switching of two-dimensional van der Waals magnets. *Nat. Mater.* **2018**, *17* (5), 406−410.
(31) Wilson, N. P.; Lee, K.; Cenker, J.; Xie, K.; Dismukes, A. H.; Telford, E. J.; Fonseca, J.; Sivakumar, S.; Dean, C.; Cao, T.; et al. Interlayer electronic coupling on demand in a 2D magnetic semiconductor. *Nat. Mater.* **2021**, *20* (12), 1657−1662.
(32) Jiang, X.; Liu, Q.; Xing, J.; Liu, N.; Guo, Y.; Liu, Z.; Zhao, J. Recent progress on 2D magnets: Fundamental mechanism, structural design and modification. *Appl. Phys. Rev.* **2021**, *8* (3), No. 031305.
(33) Guo, Y.; Zhou, S.; Zhao, J. Two-dimensional intrinsic ferromagnets with high Curie temperatures: synthesis, physical properties and device applications. *J. Mater. Chem. C* **2021**, *9* (19), 6103−6121.
(34) Liu, N.-S.; Wang, C.; Ji, W. Recent research advances in two-dimensional magnetic materials. *ACTA PHYS SIN-CH ED* **2022**, *71* (12), 127504.
(35) Li, Z.; Li, D.; Wang, H.; Chen, P.; Pi, L.; Zhou, X.; Zhai, T. Intercalation Strategy in 2D Materials for Electronics and Optoelectronics. *Small Methods* **2021**, *5* (9), No. 2100567.
(36) Li, K.; Chang, T.-H.; Xie, Q.; Cheng, Y.; Yang, H.; Chen, J.; Chen, P.-Y. Tunable Magnetic Response in 2D Materials via Reversible Intercalation of Paramagnetic Ions. *Adv. Electron. Mater.* **2019**, *5* (6), No. 1900040.
(37) Sangian, D.; Ide, Y.; Bando, Y.; Rowan, A. E.; Yamauchi, Y. Materials Nanoarchitectonics Using 2D Layered Materials: Recent Developments in the Intercalation Process. *Small* **2018**, *14* (33), No. 1800551.
(38) Jung, Y.; Zhou, Y.; Cha, J. J. Intercalation in two-dimensional transition metal chalcogenides. *Inorg. Chem. Front.* **2016**, *3* (4), 452−463.
(39) Bointon, T. H.; Khrapach, I.; Yakimova, R.; Shytov, A. V.; Craciun, M. F.; Russo, S. Approaching Magnetic Ordering in Graphene Materials by $FeCl_3$ Intercalation. *Nano Lett.* **2014**, *14* (4), 1751−1755.
(40) Song, Y.-X.; Li, Y.-Q.; Wang, L.-H.; Zhang, X.-L.; Wang, C.; Wang, Q.-S. Li intercalation modulated photocurrent response in WS_2 optoelectronic devices. *ACTA PHYS SIN-CH ED* **2023**, *72* (22), 226801.
(41) Zhou, J.; Lin, Z.; Ren, H.; Duan, X.; Shakir, I.; Huang, Y.; Duan, X. Layered Intercalation Materials. *Adv. Mater.* **2021**, *33* (25), No. 2004557.
(42) Xu, Q.-F.; Xie, W.-Q.; Lu, Z.-W.; Zhao, Y.-J. Theoretical study of enhanced ferromagnetism and tunable magnetic anisotropy of monolayer CrI_3 by surface adsorption. *Phys. Lett. A* **2020**, *384* (29), No. 126754.
(43) Yin, Y.; Lian, C.-S.; Meng, F.; Liu, Y.; Chen, W.; Ji, L.; Zhou, X.; Zhang, Z.; Zhang, Q.; Gu, L.; et al. Quenched charge density wave and large in-plane upper critical field of self-intercalated bilayer $NbSe_2$. *Phys. Rev. B* **2023**, *108* (4), No. L041405.
(44) Niu, K. D.; Qiu, G. T.; Wang, C. S.; Li, D. Y.; Niu, Y. T.; Li, S. G.; Kang, L. X.; Cai, Y. Q.; Han, M. J.; Lin, J. H. Self-Intercalated Magnetic Heterostructures in 2D Chromium Telluride. *Adv. Funct. Mater.* **2023**, *33* (2), No. 2208528.
(45) Guan, Z.; Zhang, F.; Lv, L.; Jia, C.; Wang, W.; Jiang, Y.; Li, X.; Su, Y. Tailing the Magnetoelectric Properties of 2H-MoS_2 by Engineering Covalently Bonded Mo Self-intercalation: Ferromagnetic Materials. *ACS Appl. Electron. Mater.* **2024**, *6* (66), 4066−4079.
(46) Zhao, X.; Song, P.; Wang, C.; Riis-Jensen, A. C.; Fu, W.; Deng, Y.; Wan, D.; Kang, L.; Ning, S.; Dan, J.; et al. Engineering covalently bonded 2D layered materials by self-intercalation. *Nature* **2020**, *581* (7807), 171−177.
(47) Guzman, R.; Liu, H.; Bian, C.; Bao, L.; Shen, C.-M.; Gao, H.-J.; Zhou, W. Temperature-Induced Structural Evolution and Magnetism in Self-Intercalated $V_{1+x}Se_2$ Nanoplates. *Adv. Funct. Mater.* **2024**, *34* (36), No. 2401304.
(48) Guan, Z.; Lv, L.; An, Z.; Jiang, Y.; Su, Y. Tailing the Magnetoelectric Properties of $Cr_2Ge_2Te_6$ by Engineering Covalently Bonded Cr Self-Intercalation: Ferromagnetic Half-Metal. *ACS Appl. Electron. Mater.* **2023**, *5* (6), 2999−3009.
(49) Wang, H.; Zhang, J.; Shen, C.; Yang, C.; Küster, K.; Deuschle, J.; Starke, U.; Zhang, H.; Isobe, M.; Huang, D.; et al. Direct visualization of stacking-selective self-intercalation in epitaxial $Nb_{1+x}Se_2$ films. *Nat. Commun.* **2024**, *15* (1), 2541.
(50) Wu, Q.; Quan, W.; Pan, S.; Hu, J.; Zhang, Z.; Wang, J.; Zheng, F.; Zhang, Y. Atomically Thin Kagome-Structured Co_9Te_{16} Achieved through Self-Intercalation and Its Flat Band Visualization. *Nano Lett.* **2024**, *24* (25), 7672−7680.
(51) Americo, S.; Pakdel, S.; Thygesen, K. S. Enhancing Metallicity and Basal Plane Reactivity of 2D Materials via Self-Intercalation. *ACS Nano* **2024**, *18* (6), 4746−4755.
(52) Chen, J.; Li, S.-L.; Tao, Z.-L.; Shen, Y.-T.; Cui, C.-X. Titanium Disulfide Nanotubes as Hydrogen-Storage Materials. *J. Am. Chem. Soc.* **2003**, *125* (18), 5284−5285.
(53) Whittingham, M. S. Electrical Energy Storage and Intercalation Chemistry. *Science* **1976**, *192* (4244), 1126−1127.
(54) Whangbo, M. H.; Rouxel, J.; Trichet, L. Effects of sodium intercalation in titanium disulfide on the electronic structure of a TiS_2 slab. *Inorg. Chem.* **1985**, *24* (12), 1824−1827.
(55) Lee, C.; Jeong, Y.-T.; Nogales, P. M.; Song, H.-Y.; Kim, Y.; Yin, R.-Z.; Jeong, S.-K. Electrochemical intercalation of Ca^{2+} ions into TiS_2 in organic electrolytes at room temperature. *Electrochem. Commun.* **2019**, *98*, 115−118.
(56) Butz, T.; Flagmeyer, R. H.; Jankuhn, S.; Reinert, T.; da Silva, M. F.; Soares, J. C.; Tröger, W. RBS studies of the intercalation compound Hg_xTiS_2: Morphology and staging. *NUCL INSTRUM METH B* **1998**, *136-138*, 253−257.
(57) Guilmeau, E.; Bréard, Y.; Maignan, A. Transport and thermoelectric properties in Copper intercalated TiS_2 chalcogenide. *Appl. Phys. Lett.* **2011**, *99* (5), No. 052107.
(58) Zhang, J.; Qin, X. Y.; Xin, H. X.; Li, D.; Song, C. J.; Zhang, J.; Qin, X. Y.; Xin, H. X.; Li, D.; Song, C. J. Thermoelectric Properties of Co-Doped TiS_2. *J. Electron. Mater.* **2011**, *40* (5), 980−986.
(59) Luo, J.; Xiang, G.; Tang, Y.; Ou, K.; Chen, X. The electric and magnetic properties of novel two-dimensional $MnBr_2$ and MnI_2 from first-principles calculations. *J. Appl. Phys.* **2020**, *128* (11), 113901.
(60) Zhang, M.; Zhang, C.; You, Y.; Xie, H.; Chi, H.; Sun, Y.; Liu, W.; Su, X.; Yan, Y.; Tang, X.; et al. Electron Density Optimization and

https://doi.org/10.1021/acs.jpcc.4c06216
J. Phys. Chem. C XXXX, XXX, XXX−XXX

the Anisotropic Thermoelectric Properties of Ti Self-Intercalated $Ti_{1+x}S_2$ Compounds. *ACS Appl. Mater. Interfaces* **2018**, *10* (38), 32344−32354.
(61) Beaumale, M.; Barbier, T.; Bréard, Y.; Guelou, G.; Powell, A. V.; Vaqueiro, P.; Guilmeau, E. Electron doping and phonon scattering in $Ti_{1+x}S_2$ thermoelectric compounds. *Acta Mater.* **2014**, *78*, 86−92.
(62) Wang, H.; Qiu, Z.; Xia, W.; Ming, C.; Han, Y.; Cao, L.; Lu, J.; Zhang, P.; Zhang, S.; Xu, H.; et al. Semimetal or Semiconductor: The Nature of High Intrinsic Electrical Conductivity in TiS_2. *J. Phys. Chem. Lett.* **2019**, *10* (22), 6996−7001.
(63) Kresse, G.; Furthmüller, J. Efficient iterative schemes for ab initio total-energy calculations using a plane-wave basis set. *Phys. Rev. B* **1996**, *54* (16), 11169−11186.
(64) Kresse, G.; Furthmüller, J. Efficiency of ab-initio total energy calculations for metals and semiconductors using a plane-wave basis set. *Comput. Mater. Sci.* **1996**, *6* (1), 15−50.
(65) Perdew, J. P.; Burke, K.; Ernzerhof, M. Generalized Gradient Approximation Made Simple. *Phys. Rev. Lett.* **1996**, *77* (18), 3865−3868.
(66) Heyd, J.; Scuseria, G. E.; Ernzerhof, M. Hybrid functionals based on a screened Coulomb potential. *J. Chem. Phys.* **2003**, *118* (18), 8207−8215.
(67) Liechtenstein, A. I.; Anisimov, V. I.; Zaanen, J. Density-functional theory and strong interactions: Orbital ordering in Mott-Hubbard insulators. *Phys. Rev. B* **1995**, *52* (8), R5467−R5470.
(68) Dolui, K.; Sanvito, S. Dimensionality-driven phonon softening and incipient charge density wave instability in TiS_2. *EPL* **2016**, *115* (4), 47001.
(69) Monkhorst, H. J.; Pack, J. D. Special points for Brillouin-zone integrations. *Phys. Rev. B* **1976**, *13* (12), 5188−5192.
(70) Togo, A.; Tanaka, I. First principles phonon calculations in materials science. *Scr. Mater.* **2015**, *108*, 1−5.
(71) Wang, V.; Xu, N.; Liu, J.-C.; Tang, G.; Geng, W.-T. VASPKIT: A user-friendly interface facilitating high-throughput computing and analysis using VASP code. *Comput. Phys. Commun.* **2021**, *267*, No. 108033.
(72) Lou, F.; Li, X. Y.; Ji, J. Y.; Yu, H. Y.; Feng, J. S.; Gong, X. G.; Xiang, H. J. PASP: Property analysis and simulation package for materials. *J. Chem. Phys.* **2021**, *154* (11), 114103.
(73) Nosé, S. A unified formulation of the constant temperature molecular dynamics methods. *J. Chem. Phys.* **1984**, *81* (1), 511−519.
(74) Henkelman, G.; Uberuaga, B. P.; Jónsson, H. A climbing image nudged elastic band method for finding saddle points and minimum energy paths. *J. Chem. Phys.* **2000**, *113* (22), 9901−9904.
(75) Zeng, Z.; Yin, Z.; Huang, X.; Li, H.; He, Q.; Lu, G.; Boey, F.; Zhang, H. Single-Layer Semiconducting Nanosheets: High-Yield Preparation and Device Fabrication. *Angew. Chem., Int. Ed.* **2011**, *50* (47), 11093−11097.
(76) Li, R.; Jiang, J.; Bai, H.; Mi, W. Tailoring Interlayer Magnetic Coupling to Modify the Magnetic Properties of $FeCl_2$ Bilayers by Self-Intercalation. *J. Mater. Chem. C* **2022**, *10* (40), 14955.
(77) Henkelman, G.; Arnaldsson, A.; Jónsson, H. A fast and robust algorithm for Bader decomposition of charge density. *Comput. Mater. Sci.* **2006**, *36* (3), 354−360.
(78) Goodenough, J. B. Theory of the Role of Covalence in the Perovskite-Type Manganites [La, M(II)]MnO_3. *Phys. Rev.* **1955**, *100*, 564.
(79) Anderson, P. W. New Approach to the Theory of Superexchange Interactions. *Phys. Rev.* **1959**, *115* (1), 2−13.
(80) Kanamori, J. Crystal Distortion in Magnetic Compounds. *J. Appl. Phys.* **1960**, *31* (5), S14−S23.
(81) Zhang, R.-Z.; Wan, C.-L.; Wang, Y.-F.; Koumoto, K. Titanium sulphene: two-dimensional confinement of electrons and phonons giving rise to improved thermoelectric performance. *PCCP.* **2012**, *14* (45), 15641−15644.
(82) An, Z.; Lv, L.; Su, Y.; Jiang, Y.; Guan, Z. Carrier doping modulates the magnetoelectronic and magnetic anisotropic properties of two-dimensional MSi_2N_4 (M = Cr, Mn, Fe, and Co) monolayers. *PCCP.* **2024**, *26* (5), 4208−4217.
(83) Guan, Z.; Lv, L.; An, Z.; Su, Y.; Jiang, Y.; Wu, X.; van der Ni, S. Waals Stacked 2D-Layered $Co_2Ge_2Te_6$ with High Curie Temperature and Large Magnetic Crystal Anisotropy. *J. Phys. Chem. C* **2023**, *127* (12), 5991−6001.
(84) Fu, D.; Zhao, X.; Zhang, Y.-Y.; Li, L.; Xu, H.; Jang, A. R.; Yoon, S. I.; Song, P.; Poh, S. M.; Ren, T.; et al. Molecular Beam Epitaxy of Highly Crystalline Monolayer Molybdenum Disulfide on Hexagonal Boron Nitride. *JACS.* **2017**, *139* (27), 9392−9400.
(85) Sun, L.; Yuan, G.; Gao, L.; Yang, J.; Chhowalla, M.; Gharahcheshmeh, M. H.; Gleason, K. K.; Choi, Y. S.; Hong, B. H.; Liu, Z. Chemical vapour deposition. *Nat. Rev. Methods Primers* **2021**, *1* (1), 5.

https://doi.org/10.1021/acs.jpcc.4c06216
J. Phys. Chem. C XXXX, XXX, XXX−XXX